



Dry reforming of methane over Ni/La₂O₃ nanorod catalysts with stabilized Ni nanoparticles



Xinyu Li ^{a,b}, Di Li ^{a,b}, Hao Tian ^{a,b}, Liang Zeng ^{a,b}, Zhi-Jian Zhao ^{a,b}, Jinlong Gong ^{a,b,*}

^a Key Laboratory for Green Chemical Technology of Ministry of Education, School of Chemical Engineering and Technology, Tianjin University, Tianjin 300072, China

^b Collaborative Innovation Center of Chemical Science and Engineering, Tianjin University, Tianjin 300072, China

ARTICLE INFO

Article history:

Received 17 July 2016

Received in revised form

21 September 2016

Accepted 28 September 2016

Available online 29 September 2016

Keywords:

Hexagonal lanthanum dioxygenate

Dry reforming of methane

Ni catalysts

Anti-sintering

Nanorod-shaped metal oxide

ABSTRACT

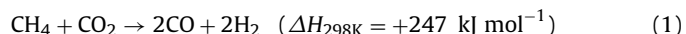
This paper describes the design of a Ni/La₂O₃ catalyst using La₂O₂CO₃ nanorod as a support precursor (denoted as Ni/La₂O₃-LOC) via a wet impregnation method for dry reforming of methane (DRM). The results showed that La₂O₃ derived from the La₂O₂CO₃ precursor maintained its initial morphology upon thermal treatment and could highly disperse Ni particles on it. Additionally, the nanorod-shaped support could provide more medium-strength basic sites to facilitate CO₂ adsorption and activation on its surface. Consequently, the Ni/La₂O₃-LOC catalyst reached 70% of CH₄ conversion and 75% of CO₂ conversion at 700 °C after 50 h DRM reaction with a H₂/CO ratio of 0.87. The enhanced metal-support interaction restricted the sintering of nickel particles under harsh reaction conditions. Coke evolution on the catalysts was also investigated to understand coke formation mechanism and the role of La₂O₂CO₃ in coke elimination. It has been found that nickel dispersion can affect distribution of coke and La₂O₂CO₃ on the surface of catalyst, both of which have a close relation with catalytic performance.

© 2016 Elsevier B.V. All rights reserved.

1. Introduction

With the rapid development of human society, people rely on energy more than ever before. As one of the three primary fossil fuels (coal, oil and natural gas), the exploitation of natural gas is increasing, which requires clean and efficient utilization of methane. Simultaneously, discoveries of abundant shale gas reserves are expected to reduce dependence on crude oil [1]. At present, industrial-scale hydrogen generation is still dependent on the conversion of natural gas or shale gas [2], and methane reforming processes have been extensively investigated [3–5], such as steam reforming of methane (SRM) [6], partial oxidation of methane (POM) [7–9], autothermal reforming of methane (ATR) [10], and dry reforming of methane (DRM) [11]. DRM has many intriguing advantages attracting considerable attention [3]. DRM (Eq. (1)) uses CH₄ and CO₂ as feedstocks to produce syngas (CO + H₂) so that DRM can mitigate the adverse effect resulting from global warming problems, since both CH₄ and CO₂ are major greenhouse gases. On the other hand, the obtained syngas via DRM process has a moderate ratio of H₂ to CO (1:1), which is lower than the syngas

obtained via SRM process (H₂/CO = 3:1), and then the mixture of the above two syngases can be applied in liquid fuel production through the Fischer-Tropsch synthesis (H₂/CO = 2:1) [10,12,13]. Moreover, CO₂ is an undesirable impurity in natural gas and sometimes its concentration is as high as 70% [14,15]. The raw natural gas can be directly used as DRM feedstock to produce syngas so that subsequent gas separation and purification can be cut to save equipment investment. However, the obtained syngas via DRM process generally has a ratio of H₂/CO lower than 1 due to the occurrence of reverse water gas shift (RWGS) reaction (Eq. (2)) [3], which is harmful for H₂ production since a part of H₂ reacts with the reactant CO₂ to produce water [16]. RWGS is thermodynamically favored at low temperatures (<600 °C) [17,18], thus DRM is typically operated at 700–800 °C to suppress RWGS and coke from the Boudouard reaction (Eq. (3)) for attaining industrial relevant conversions [19–21]. Moreover, when temperature reaches beyond 800 °C, sintering occurs significantly and the process is highly energy-consuming [19].



* Corresponding author at: 92 Weijin Road, Nankai District, School of Chem. Eng. & Technol., Tianjin University, China.

E-mail address: jlgong@tju.edu.cn (J. Gong).

Active metals of catalysts used in DRM can be generally divided into noble metals [3] and base metals [4]. Noble metals primarily comprise Pt [22], Rh [11], Ru [23], etc., which have superior capacity to cleave the C–H bond and suppress carbon deposition. However, their industrial application is restricted due to their high costs. Simultaneously, nickel-based catalysts have been extensively investigated in the DRM process on account of their high catalytic activity and availability. Nickel-based catalysts have two intrinsic drawbacks which can result in deactivation: they are prone to sinter under elevated temperatures and suffer from severe coke deposition. Coke deposition mainly originates from the Boudouard reaction (Eq. (3)) and CH₄ decomposition (Eq. (4)) [24]. There are various mechanisms to suppress sintering and coke deposition [4]. Our group recently summarized encapsulated group VIII metal catalysts exhibiting excellent anti-sintering performance [25]. In addition, Liu et al. concluded various types of carbon deposition and respective carbon growth mechanism on nickel-based catalysts used in the DRM process [5].

The reaction mechanism of DRM depends on the properties of both active metals and supports. Iglesia et al. extensively studied the mechanism of CH₄ reforming reactions on the basis of isotopic and kinetic assessment [26–28]. Up till now, many oxides have been investigated in DRM to support nickel nanoparticles, such as Ni/SiO₂ [29,30], Ni/Al₂O₃ [31], and Ni/La₂O₃ [7–9,32,33]. For Ni/SiO₂, both CH₄ and CO₂ are activated on metal active sites [4], where the monofunctional mechanism will cause two reactants to compete for metal active sites thus leading to the decrease of reaction rates. With regard to Ni/La₂O₃, it follows a bifunctional mechanism: methane dissociation occurs on Ni nanoparticles, which is typically considered as the rate determining step, and CO₂ activation occurs on La₂O₃ support [34–36]. Generally, supports with acidity are more inclined to cause coke deposition [4], while La₂O₃ as a basic support can promote CO₂ adsorption and activation on its surface since CO₂ has mild acidity [37]. Indeed, La₂O₃ is applied in DRM for its basicity and its capacity to react with CO₂ to form La₂O₂CO₃, both of which are advantageous to suppress carbon deposition. La₂O₂CO₃ can react with coke on the surface of nearby Ni nanoparticles (NPs) to form CO and regenerate La₂O₃ [34–36,38]. Recently, Müller and co-workers reported that the addition of Co on Ni/La₂O₃ can increase the rate of La₂O₂CO₃ formation and bring about improvements in catalytic activity and stability [33]. Therefore, La₂O₂CO₃ is regarded as a good intermediate species to eliminate deposited coke.

Poor dispersion of active metal on La₂O₃ is the main problem for Ni/La₂O₃-based catalysts due to the limited surface area [39]. In order to improve this problem, mineral-type precursors are introduced in this system, such as perovskite [39,40], spinel [41], pyrochlore [11,15]. LaNiO₃ perovskite derived Ni/La₂O₃ has been studied extensively [42], on which Ni dispersion gained prominent improvement. Additionally, a method of nanocasting using SBA-15 as a hard template was adopted to prepare high-surface-area LaNiO₃ perovskite precursor, which could further disperse Ni particles on La₂O₃ support after reduction [37]. However, a common drawback of this method is that the introduced template is hard to remove completely [43]. Mo et al. adopted oleic acid in the impregnated solution to disperse Ni particles on La₂O₃ doped SiO₂ support via a self-assembled core-shell precursor route [44]. Besides, La₂O₃ is usually used as promoter due to the fact that La₂O₃ can improve catalyst properties including surface basicity of supports and metal-support interaction. Montero et al. used La₂O₃ as promoter to investigate coke formation mechanism during the deactivation of a Ni/La₂O₃–α-Al₂O₃ catalyst in ethanol steam reforming (ESR) process, since La₂O₃ can tune surface basicity of support to suppress the formation of C₂H₄ as coke precursor [45]. Our group found La-modifiers enhanced the basicity of ordered mesoporous Ni-based catalysts, suppressed carbon deposition and

improved catalyst stability [46]. However, on account of intrinsic hydrophilic nature of La₂O₃, La species may partially cover the Ni catalytic surface via the migration of La species and then lead to the deactivation of catalysts [47]. Therefore, the amount of La₂O₃ addition should be controlled.

La₂O₂CO₃ as an active intermediate of La₂O₃ to suppress deposited coke can be easily prepared with different shapes, such as nanorods, nanoplates, nanosheets, nanoparticles, nanoflowers [43]. Among nanoshaped La₂O₂CO₃, La₂O₂CO₃ nanorods have been applied in steam reforming of glycerol [48] and oxidative coupling of methane [49], which can enhance interaction with metals thus exhibiting excellent anti-sintering performance [50,51]. Recently, Singh et al. found that Ni/La₂O₃ highly depends on shape and structure of parent nanoparticles [32]. Moreover, they reported that high-aspect ratio parent shapes (e.g. rods) may prove to be an ideal structure [32].

This paper describes the synthesis of Ni/La₂O₃ nanorod catalyst with stabilized Ni nanoparticles for the DRM process. We expect that nanorod-shaped La₂O₂CO₃ as a support precursor could enhance Ni dispersion on La₂O₃ support and contribute to obtain robust DRM performance. Coke evolution was investigated to understand coke mechanism on Ni/La₂O₃ catalyst and the role of La₂O₂CO₃ in coke elimination. The physical-chemical properties of the catalysts were investigated by X-ray diffraction (XRD), N₂-adsorption, transmission electron microscopy (TEM), H₂ pulse chemisorption, thermogravimetric analysis (TGA), H₂ temperature-programmed reduction (H₂-TPR), temperature-programmed oxidation (TPO), and Raman spectra. Catalytic tests were conducted to differentiate the performance of the two catalysts. The stabilities of the both catalysts were characterized under high gas hourly space velocity (GHSV), while low GHSV was adopted to investigate the coke evolution on the catalysts.

2. Experimental

2.1. Catalyst preparation

Analytical grade Ni(NO₃)₂·6H₂O and La(NO₃)₃·6H₂O were obtained from Aladdin Industrial Corporation (Shanghai, China). De-ionized water (18.0 MΩ) was prepared from Ulupure water purifier machine (Chengdu, China). Anhydrous ethanol (99.8 wt.%) and analytical grade aqueous ammonia (25 wt.%) were supplied by Guangfu Fine Chemical Research Institute (Tianjin, China). Guaranteed grade urea was gained from Kermel Chemical Reagent (Tianjin, China).

The synthesis routes of La₂O₂CO₃ are modified according to the preparation method reported by Huang et al. [48]. 2.6 g of La(NO₃)₃·6H₂O was dissolved in 160 mL of de-ionized water, and 7.2 g of urea was dissolved in another 240 mL of de-ionized water. Once dissolved, the two solutions were mixed with continuously stirring, and then 1.6 mL of aqueous ammonia was added into the mixture. After heating in a water bath at 90 °C for 3 h with agitation, the obtained white suspension was naturally cooled to room temperature. Then the white suspension was centrifuged, and the precipitate was washed twice with absolute ethanol. After drying at 80 °C overnight and calcination at 500 °C for 2 h, nanorod-shaped La₂O₂CO₃ was obtained.

Ni/La₂O₃ catalysts were prepared by a wet impregnation method. The loading was fixed to 5 wt% for all the reduced samples to be investigated. The supported Ni/La₂O₃ catalyst was prepared by impregnating 0.95 g of La₂O₂CO₃ with an aqueous solution containing 0.25 g of Ni(NO₃)₂·6H₂O dissolved in 40 mL of de-ionized water. After stirring at 80 °C for 3 h, vacuum evaporation was carried out until the solvent was completely removed. Then the sample was ground and calcined at 600 °C for 2 h.

After ground into 20–40 mesh, the sample was reduced at 700 °C under H₂ atmosphere (H₂/N₂ = 1:3, 40 mL/min) for 1.5 h, during which La₂O₂CO₃ would mainly transform into La₂O₃. The prepared Ni/La₂O₃ nanorod catalyst was marked as 5Ni/La₂O₃-LOC, where LOC denotes that La₂O₃ is derived from La₂O₂CO₃.

A reference Ni/La₂O₃ catalyst containing the same Ni loading was synthesized with a similar procedure. Here La₂O₃ was obtained via calcination of La(NO₃)₃·6H₂O at 800 °C for 2 h, and subsequent procedures follow as the above. The prepared catalyst was named as 5Ni/La₂O₃-C, where C denotes that La₂O₃ is prepared through conventional synthesis routes [39].

2.2. Characterization

Data with regard to textural properties of catalysts were collected from nitrogen adsorption-desorption at –196 °C by utilizing a Micromeritics Tristar 3000 analyzer. All materials needed to be degassed at 300 °C for 3 h prior to the tests. The Brunauer-Emmett-Teller (BET) method was applied to figure out the specific surface areas on the basis of the N₂ isotherms. And the Barret-Joyner-Halenda (BJH) method was adopted to figure out the cumulative volumes of pores from the desorption branches of the N₂ isotherms.

The inductively coupled plasma optical emission spectroscopy (ICP-OES) (VISTA-MPX, Varian) was applied to examine elemental contents in the prepared catalysts. The samples were dissolved in nitric acid solutions prior to measurements.

XRD patterns were examined with 2θ values ranging from 10° to 80°, utilizing a Rigaku D/max-2500 diffractometer equipped with the graphite filtered Cu Kα radiation ($\lambda = 1.54056 \text{ \AA}$). The mean crystalline size of Ni particles was calculated by the Scherrer's equation on the basis of the diffraction peaks corresponding to the Ni (111) facet.

H₂-TPR experiment was measured on a chemisorption apparatus (Micromeritics AutoChem II 2920) in order to analyze the reduction behavior of the catalysts. Typically, the sample (100 mg) was pretreated at 300 °C for 1 h under an Ar stream (30 mL/min) aiming to remove moisture and impurities. Afterwards the system was cooled to 50 °C, and then a 10 vol% H₂/Ar stream (30 mL/min) was introduced for reduction. Subsequently, the temperature was programmed to raise linearly from 100 °C to 900 °C with a rate of 10 °C/min and signal of the thermal conductivity detector (TCD) was recorded.

CO₂-TPD analysis was performed on the same chemisorption apparatus (Micromeritics AutoChem II 2920) to investigate the basicity of the catalyst. The sample (100 mg) was prereduced at 750 °C for 0.5 h under a 10 vol% H₂/Ar stream (50 mL/min). Afterwards the system was cooled to 60 °C, and then a stream of CO₂ gas (50 mL/min) was introduced. Subsequently, a stream of He gas (30 mL/min) was introduced and the temperature was scheduled to increase to 120 °C to remove CO₂ residue in stream. When the baseline of CO₂ signal in TCD maintained stable, the temperature was programmed to increase from 120 °C to 900 °C with a ramping rate of 10 °C/min and TCD signal was recorded at the same time.

TPO experiment was performed on the same chemisorption apparatus (Micromeritics AutoChem II 2920) in order to study the properties of deposited coke on catalysts. Herein, a mass spectrometer (MS) (HIDEN QIC-20) was connected to the chemisorption apparatus. The spent catalyst (10 mg) was pretreated at 150 °C for 0.5 h under an Ar stream (30 mL/min) to remove moisture and impurities. After the system was cooled to 50 °C, a 10 vol% O₂/He stream (30 mL/min) was introduced for oxidation. Simultaneously, the temperature was programmed to increase linearly from 50 °C to 900 °C with a ramping rate of 10 °C/min. The CO₂ (*m/z*=44) and CO (*m/z*=28) in the outlet gas was detected and recorded online by the MS.

H₂ pulse chemisorption was measured on the same chemisorption apparatus (Micromeritics AutoChem II 2920) in order to figure out the nickel active surface area. The catalyst was prereduced at 700 °C for 1 h under a 10% H₂/Ar flow (30 mL/min), and then it was cooled to 50 °C under an Ar stream (30 mL/min). After that, H₂ pulses were injected until the eluted peak area of consecutive pulses remained stable. Therefore, the active surface area of nickel particles was calculated from the volume of adsorbed H₂, according to the assumption that the stoichiometry of H/Ni_s (surface nickel atom) is 1 and the surface area per Ni atom is $6.5 \times 10^{-20} \text{ m}^2$ [52].

The morphology and structure of catalysts was examined by utilizing a TEM instrument (FEI Tecnai G2 F20) under a working voltage of 100 kV. Devices for high-resolution electron energy-loss spectroscopy (EELS) was also connected to the microscope to carry out elemental analysis. Prior to the test, sample powder needed to be dispersed in absolute ethanol via ultrasonication. Afterwards, the suspension was dripped onto a copper grid-supported transparent carbon foil and dried in air before TEM images were recorded.

TGA was conducted to investigate the properties of deposited coke on spent catalysts with application of a TGA system (STA449F3, NETZSCH Corp.). The TGA experiment was conducted under an air stream (50 mL/min), and temperature was lifted from room temperature to 1000 °C with a heating rate of 10 °C/min. Finally, the amount of coke deposition was calculated from the mass loss in TGA profiles, excluding oxidation of Ni particles and decomposition of La₂O₂CO₃.

Raman spectra were obtained from a Raman spectrometer (Renishaw inVia Reex) equipped with a 532 nm Ar-ion laser beam. Here, Raman spectra was collected under ambient conditions.

2.3. Catalytic test

Catalytic activity tests were performed in a quartz fixed-bed tubular reactor ($\Phi 8 \times 44 \text{ mm}$) under atmospheric pressure. Typically, 100 mg of catalyst sample (20–40 mesh) was evenly mixed with 1 mL of quartz particles and then loaded inside the reactor. Prior to the test, the catalysts were reduced at 700 °C for 1.5 h under a 25 vol% H₂/N₂ stream (40 mL/min). The feed gas flow rate to the reactor was set at 100 mL/min (GHSV = 60,000 mL h⁻¹ g_{cat}⁻¹, CH₄:CO₂:N₂ = 15:15:70) aiming to expand the difference in activity between the two catalysts. Here, GHSV is based on total flow. A gas chromatograph (GC2060, Shanghai Ruimin Instrument) adopting He as the carrier gas was applied to analyze the gas species online including CH₄, CO₂, H₂, CO, and N₂. The GC was equipped with a TCD and two columns, of which a TDX-01 column was followed by a 5A molecular sieve column. In activity test, the reaction temperature was programmed to decrease from 700 °C to 500 °C with an interval of 50 °C, and the activity data were collected under steady-state conditions. Typically, conversions are controlled to be remarkably lower than thermodynamic equilibrium conversions in order to calculate TOF values [53]. Besides, stability test was performed at 700 °C. In addition, GHSV was decreased to 30,000 mL h⁻¹ g_{cat}⁻¹ to investigate the evolution of carbon formation.

CH₄, CO₂ conversions (X_{CH_4} and X_{CO_2}), selectivity to H₂ and CO (S_{H_2} and S_{CO}), and the H₂/CO ratio are defined as follows:

$$X_{\text{CH}_4} = \frac{F_{\text{CH}_4, \text{ in}} - F_{\text{CH}_4, \text{ out}}}{F_{\text{CH}_4, \text{ in}}} \quad (5)$$

$$X_{\text{CO}_2} = \frac{F_{\text{CO}_2, \text{ in}} - F_{\text{CO}_2, \text{ out}}}{F_{\text{CO}_2, \text{ in}}} \quad (6)$$

$$S_{\text{H}_2} = \frac{F_{\text{H}_2, \text{ out}}}{2 \times (F_{\text{CH}_4, \text{ in}} - F_{\text{CH}_4, \text{ out}})} \quad (7)$$

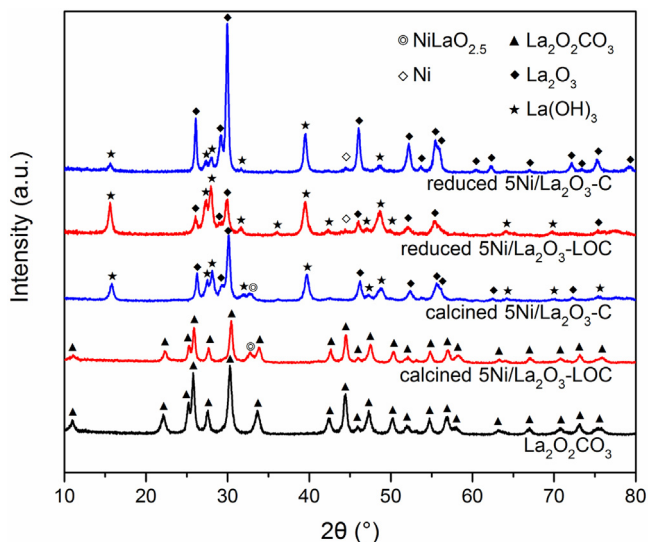


Fig. 1. XRD patterns of the calcined and reduced catalysts.

Table 1
H₂ consumption values for TPR experiments.

Sample	Peak	H ₂ consumption (mmol/g _{cat})	Percentage of total H ₂ consumption (%)	Degree of catalyst reduction (%) ^a
5Ni/La ₂ O ₃ -C	293	0.22	38	60
	528	0.36	62	
5Ni/La ₂ O ₃ -LOC	339	0.68	74	88
	547	0.24	26	

^a Determined by the ratio of practical H₂ consumption to theoretical H₂ consumption.

$$S_{\text{CO}} = \frac{F_{\text{CO, out}}}{(F_{\text{CH}_4, \text{ in}} - F_{\text{CH}_4, \text{ out}}) + (F_{\text{CO}_2, \text{ in}} - F_{\text{CO}_2, \text{ out}})} \quad (8)$$

$$\text{H}_2/\text{CO} = \frac{F_{\text{H}_2, \text{ out}}}{F_{\text{CO, out}}} \quad (9)$$

3. Results and discussion

3.1. Characterization of calcined catalysts

Diffraction patterns of calcined catalysts are presented in Fig. 1. The pattern of as-prepared La₂O₂CO₃ is assigned to hexagonal lanthanum dioxycarbonate (JCPDF: 37-0804). Upon calcination at 600 °C, La₂O₂CO₃ remains stable for the calcined 5Ni/La₂O₃-LOC. It was reported that hexagonal La₂O₂CO₃ kept stable up to 750 °C [48]. On the other hand, La(OH)₃ (JCPDF: 36-1481) forms on the calcined 5Ni/La₂O₃-C due to the combination of La₂O₃ (JCPDF: 05-0602) and H₂O produced from decomposition of Ni(NO₃)₂·6H₂O during the calcination step. In addition, formation of NiLaO_{2.5} (JCPDF: 49-1011) is detected on the both calcined catalysts (Fig. 1).

H₂-TPR profiles of the calcined catalysts are shown in Fig. 2 and quantification of H₂-TPR data are summarized in Table 1 to compare the reduction behavior of the calcined catalysts. For H₂-TPR profile of La₂O₂CO₃, two peaks at around 456 °C and 746 °C are caused by the decomposition of La₂O₂CO₃ [48], which can release CO₂ to react with H₂. The lower peak is ascribed to the surface of La₂O₂CO₃, while the higher peak corresponds to the bulk of La₂O₂CO₃ [48]. It was reported that La₂O₃ reduction by H₂ occurred at extremely high temperatures (above 900 °C) [54]. Therefore, no peaks are observed corresponding to La₂O₃ reduction. For 5Ni/La₂O₃-LOC, the peak centered at 745 °C is attributed to the decomposition of La₂O₂CO₃. In order to compare 5Ni/La₂O₃-LOC with 5Ni/La₂O₃-C

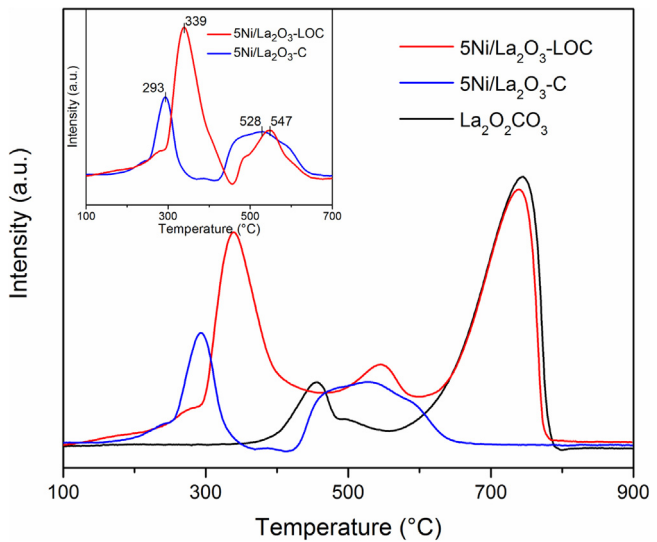


Fig. 2. H₂-TPR profiles of the calcined catalysts and corresponding baseline subtracted profile of the calcined 5Ni/La₂O₃-LOC (inset).

accurately, the H₂-TPR profile of pure La₂O₂CO₃ has been collected and used as a baseline, and then the baseline-subtracted profile of 5Ni/La₂O₃-LOC could be seen in the inset of Fig. 2. For both catalysts, mainly two reduction peaks were detected below 700 °C. The former corresponds to the reduction of bulk NiO [55,56], and the latter is assigned to the reduction of NiLaO_{2.5} phase [39]. It is noteworthy that with regard to both categories of peaks, the reduction temperature of 5Ni/La₂O₃-LOC is higher than that of 5Ni/La₂O₃-C, suggesting that the interaction between metal and support on 5Ni/La₂O₃-LOC is enhanced. In addition, the average size of Ni particles supported on 5Ni/La₂O₃-LOC (12.6 nm) is smaller than that on 5Ni/La₂O₃-C (17.3 nm) as shown in Table 2. For 5Ni/La₂O₃-LOC, 74% of the total H₂ consumption was used to reduce Ni species with lower reduction temperature, while for 5Ni/La₂O₃-C this percentage takes up merely 38%. This remarkable difference indicates that 5Ni/La₂O₃-LOC exposes more nickel active sites accessible to reduction and can gain higher active metal dispersion [57]. Moreover, the degree of catalyst reduction presented in Table 1 can be calculated according to the ratio of the practical H₂ consumption to theoretical H₂ consumption. Due to hydrophilicity of La₂O₃, some part of nickel element can be embedded into La₂O₃ matrix and covered by La₂O₃ so that eventually it cannot be reduced by H₂ [47]. The reduction degree of 5Ni/La₂O₃-LOC is 88%, higher than that of 5Ni/La₂O₃-C (60%). The effect of this difference on catalyst performance will be discussed later on.

It has to be mentioned that different calcination temperatures (500 °C, 600 °C and 700 °C) have also been investigated in order to demonstrate that calcination temperature can influence the proportion of NiO and NiLaO_{2.5} on calcined catalysts (Fig. S1). As calcination temperature increases, the content of NiO becomes much lower and the content of NiLaO_{2.5} becomes significantly higher. Additionally, the reduction temperature of NiLaO_{2.5} increases with the calcination temperature. It has been verified above that the reduction degree relies on the proportion of NiO and NiLaO_{2.5}, which will affect both particle size and dispersion of Ni NPs on reduced catalysts (shown in Section 3.2). According to Valle et al., for Ni/La₂O₃-αAl₂O₃ catalyst, both calcination temperatures and reduction temperatures could remarkably affect the amount and nature of the active metal dispersed on the support [58]. Thus, correlation between calcination-reduction temperatures can greatly affect the performance of the catalyst during the reforming process

Table 2

Textural properties of the reduced/spent catalysts and calcined pure supports.

Sample	BET surface area (m^2/g)	Average pore diameter (nm)	Pore volume (cm^3/g)	Ni content (wt%) ^a	Particle size of Ni (nm)	Ni surface area ($\text{m}^2/\text{g}_{\text{Ni}}$) ^d
5Ni/La ₂ O ₃ -C	9.2	18.3	0.08	5.7	17.3 ^b /30.1 ^c	0.51/0.19
5Ni/La ₂ O ₃ -LOC	23.0	27.4	0.17	6.1	12.6/13.8	3.27/2.99
La ₂ O ₃ -C	11.2	18.5	0.09	N/A	N/A	N/A
La ₂ O ₂ CO ₃	58.9	24.8	0.19	N/A	N/A	N/A

^a Determined by ICP-OES.

^b Determined from Scherrer's equation from the (111) plane of nickel of reduced catalysts in XRD patterns.

^c Determined by size distribution of Ni particles on spent catalysts after 50 h DRM reaction in TEM images.

^d Determined by H₂ pulse chemisorption, reduced catalyst/spent catalyst after 50 h DRM reaction.

[58]. Herein, activity tests indicate that when both reduction temperature and reaction temperature are fixed at 700 °C, the catalyst calcined at 500 °C deactivates rapidly, while the catalyst calcined at 700 °C possesses much lower activity than the catalyst calcined at 600 °C (not shown). Therefore, calcination temperature is fixed at 600 °C while reduction temperature is fixed at 700 °C.

3.2. Characterization of reduced catalysts

Table 2 sums up the textural properties of the both reduced catalysts. 5Ni/La₂O₃-LOC has slightly higher BET surface area (23.0 m²/g) than 5Ni/La₂O₃-C (9.2 m²/g), but its Ni surface area is prominently larger than that of 5Ni/La₂O₃-C. One reason for this salient difference is that La₂O₂CO₃ nanorod as support precursor has higher BET surface area (58.9 m²/g) than La₂O₃ prepared through conventional routes (11.2 m²/g) so that La₂O₂CO₃ nanorod can improve nickel dispersion on it [37]. For 5Ni/La₂O₃-LOC, its decrease of BET surface area upon reduction is mainly ascribed to hydrophilic nature of lanthanum oxygenate [37], which are caused by the presence of water molecules under increased temperature. Additionally, the notable difference of Ni surface area between the two catalysts is consistent with H₂-TPR results that 5Ni/La₂O₃-LOC is more accessible to reduction than 5Ni/La₂O₃-C.

XRD patterns of the reduced catalysts are also presented in **Fig. 1**. For both catalysts, the support mainly transforms into La₂O₃ partly mixed with La(OH)₃, but the proportion of La(OH)₃ on 5Ni/La₂O₃-LOC is higher than that on 5Ni/La₂O₃-C. The increase of La(OH)₃ proportion on the support can enhance the concentration of surface-adsorbed hydroxyl groups, which in turn can promote CO₂ adsorption on the support [46]. In addition, nickel crystallite size on the basis of diffraction peaks of Ni (111) facet ($2\theta = 44.5^\circ$) and Scherer's equation are exhibited in **Table 2**. It can be observed that 5Ni/La₂O₃-LOC (12.6 nm) presents smaller nickel particle size than 5Ni/La₂O₃-C (17.3 nm), which is in line with the result of H₂ pulse chemisorption that 5Ni/La₂O₃-LOC (3.27 m²/g_{Ni}) has higher active metal surface area than 5Ni/La₂O₃-C (0.51 m²/g_{Ni}).

CO₂-TPD is applied to investigate the basicity of the two reduced catalysts as shown in **Fig. 3**. Since CO₂ has mild acidity, basic supports are beneficial for CO₂ to adsorb on the surface [46]. According to the result of XRD (**Fig. 1**), La₂O₂CO₃ nanorod promotes the formation of La(OH)₃ on the surface of the reduced 5Ni/La₂O₃-LOC, which can increase hydroxyl groups on the surface of the support to strengthen CO₂ adsorption. As indicated in **Fig. 3** and **Table 3**, four types of basic sites can be divided on the basis of CO₂ desorption temperature range and they are marked as Type I, II, III, IV. Compared with 5Ni/La₂O₃-C, the increase of basic sites for 5Ni/La₂O₃-LOC mainly comes from the increment of basic sites with higher desorption temperature. It should be mentioned that if the increase of basic sites merely resulted from the increase of surface area, all of four types of basic sites would be proportional to the surface area. For the third and fourth type of basic sites, the temperature range is mainly between 300 and 700 °C, which corresponds to the medium-strength basic sites [59,60]. Therefore, 5Ni/La₂O₃-

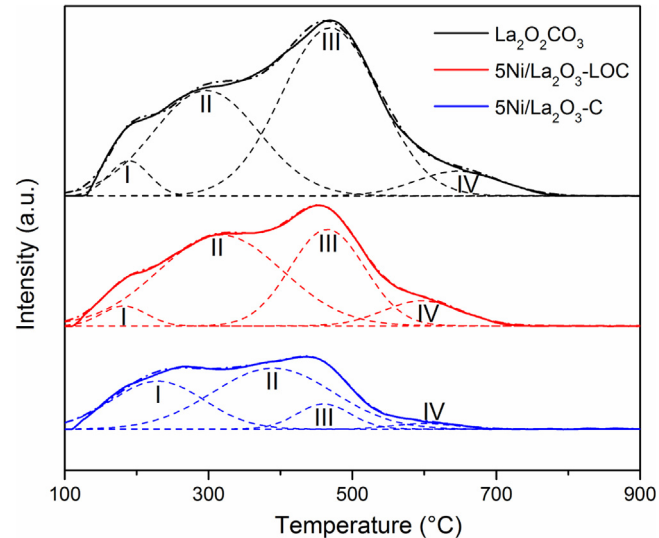


Fig. 3. CO₂-TPD profiles of the reduced catalysts.

LOC possesses more medium-strength basic sites compared with 5Ni/La₂O₃-C.

Fig. 4 shows the TEM micrographs of the reduced catalysts. For 5Ni/La₂O₃-LOC as shown in **Figs. 4a** and 4b, the nanorod shape maintains after calcination and reduction. It has been reported that lanthanum hydroxycarbonate (LaCO₃OH) prepared with specific morphology can be easily converted to La₂O₂CO₃ and La₂O₃ with the initial morphology after annealing at appropriate temperatures [43]. As shown in **Fig. 4d** and e, nickel particles on the 5Ni/La₂O₃-LOC have small sizes, which agrees with the results of XRD patterns (**Table 2**) and these nickel particles mainly expose (111) facets. While for 5Ni/La₂O₃-C (**Fig. 4c** and f), some Ni particles are covered by La₂O₃ due to its hydrophilicity, which could lead to the decrease of Ni surface area. Additionally, lanthanum oxygenates on 5Ni/La₂O₃-LOC expose {110} facets. It has been reported that the {110} planes of La₂O₂CO₃ could provide more medium-strength basic sites [48,60]. As confirmed by the result of CO₂-TPD (**Fig. 3**), nanorod-shaped support of 5Ni/La₂O₃-LOC indeed possesses more medium-strength basic sites after reduction.

EELS mapping technique is performed in order to characterize the element distribution patterns of the catalysts and nickel mapping is displayed in **Fig. 5b** and d. As shown in **Fig. 5a** and b, nickel particles with small size are evenly distributed along with nanorod-shaped support of 5Ni/La₂O₃-LOC, while nickel dispersion is relatively poor for 5Ni/La₂O₃-C and large nickel (~40 nm) particles can be observed in **Fig. 5c** and d. For 5Ni/La₂O₃-C, the occurrence of sintering upon reduction is mainly due to its weak metal-support interaction as verified in results of TPR (**Fig. 2**) and is consistent with its lower Ni surface area (**Table 2**).

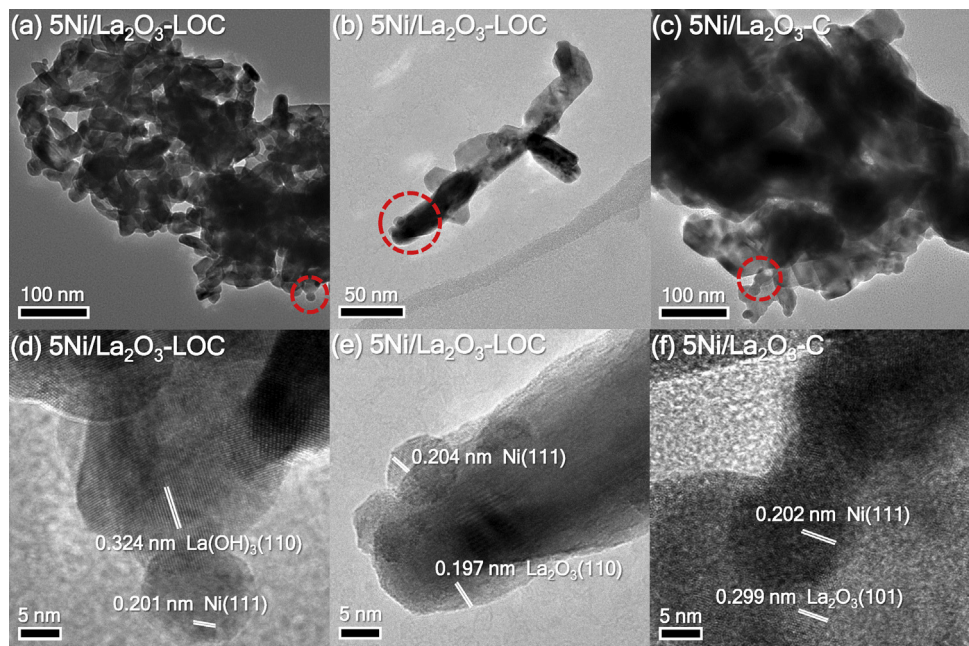


Fig. 4. TEM images of reduced (a,b,d,e) 5Ni/La₂O₃-LOC (c,f) 5Ni/La₂O₃-C catalysts.

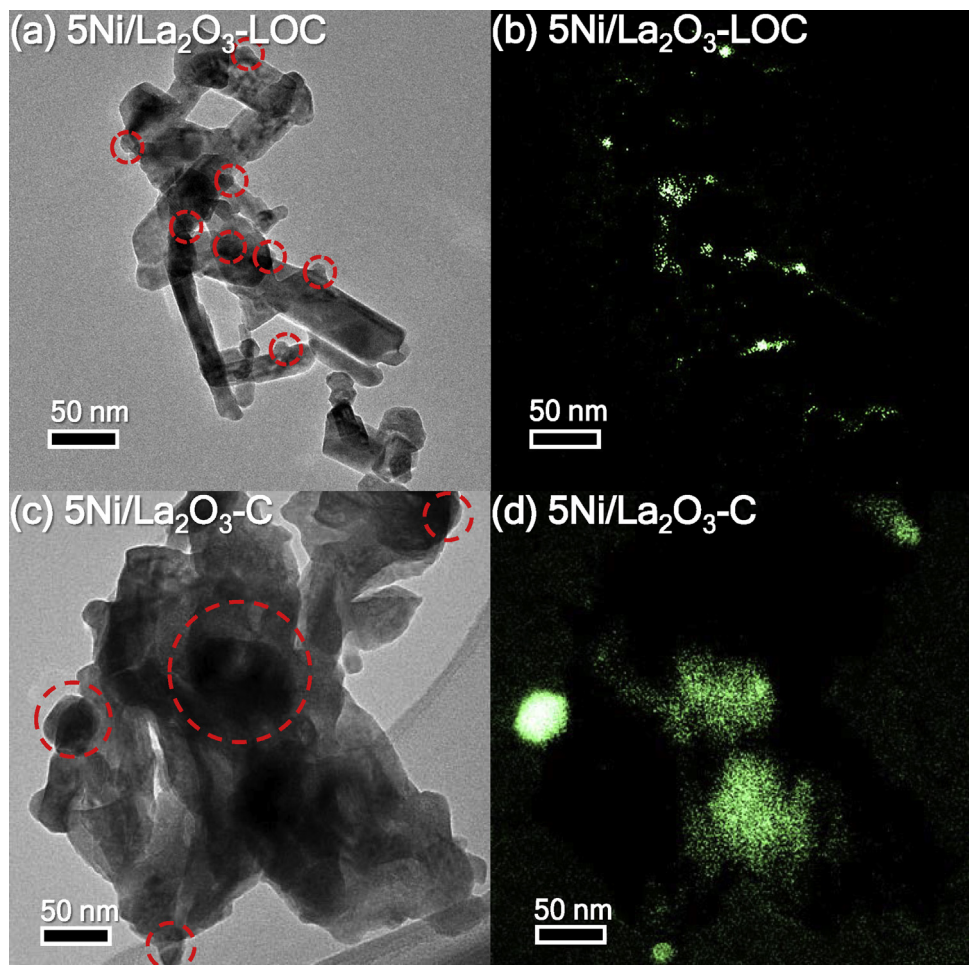


Fig. 5. TEM images and corresponding EELS mapping of the reduced catalysts, with green pixels for nickel element. (a,b) 5Ni/La₂O₃-LOC (c,d) 5Ni/La₂O₃-C. (For interpretation of the references to colour in this figure legend, the reader is referred to the web version of this article.)

Table 3

Amounts of basic sites of catalysts based on CO₂-TPD measurements.

Sample	CO ₂ adsorption (mmol/g _{cat})					Total
	Type I	Type II	Type III	Type IV		
La ₂ O ₂ CO ₃	0.026	0.204	0.301	0.039	0.570	
5Ni/La ₂ O ₃ -LOC	0.017	0.211	0.136	0.037	0.401	
5Ni/La ₂ O ₃ -C	0.084	0.142	0.026	0.008	0.260	

Table 4

Quantitative calculation of methane conversion rates.

Catalyst	T °C	GHSV L g _{cat} ⁻¹ h ⁻¹	X _{CH4,0}	X _{CH4} %	Ni _w wt.%	H ₂ uptakes mmol g _{cat} ⁻¹	CH ₄ conversion rate		
							mmol g _{cat} ⁻¹ s ⁻¹	mmol g _{Ni} ⁻¹ s ⁻¹	TOF (s ⁻¹)
5Ni/La ₂ O ₃ -LOC	700	300	0.15	23.6	5.7	5.13 × 10 ⁻³	0.132	2.31	12.8
5Ni/La ₂ O ₃ -C	700	300	0.15	3.7	6.1	0.80 × 10 ⁻³	0.021	0.34	12.9
5Ni/La ₂ O ₃ -LOC	700	60	0.15	70	5.7	5.13 × 10 ⁻³	0.078	1.37	7.6
Nanocast-Ni/La ₂ O ₃ [37]	700	30	0.20	80	26.6	N/A	0.060	0.22	N/A

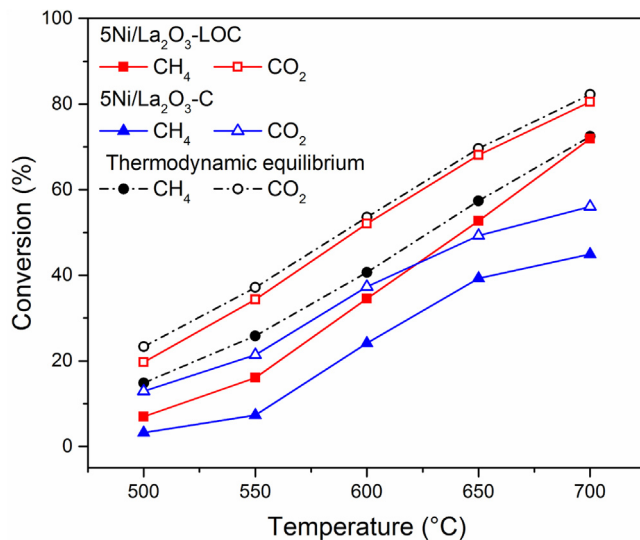


Fig. 6. DRM activity of the catalysts. Reaction conditions: CH₄/CO₂/N₂ = 15/15/70 mL/min, GHSV = 60,000 mL h⁻¹ g_{cat}⁻¹, 1 atm.

3.3. Catalytic performance in DRM

The activity data were collected under steady-state conditions, and the results are shown in Fig. 6. As the reaction temperature increases, the activities of both catalysts raise and the difference in activities is becoming larger since DRM is an endothermal reaction. The activity of 5Ni/La₂O₃-LOC is significantly higher than that of 5Ni/La₂O₃-C at 700 °C and approaches thermodynamic equilibrium (calculated by Equilibrium Composition Block of HSC software, version 6.0). It should be noted that this thermodynamic equilibrium consists of DRM reaction, RWGS reaction and coke deposition. In addition, the catalysts do not change in the course of measurements when temperature is lowered and then raised. (Fig. S2) For both catalysts, CO₂ conversion is slightly higher than CH₄ conversion due to the occurrence of RWGS reaction [3]. The obvious difference in CH₄ conversion between the two catalysts is ascribed to the higher nickel dispersion of 5Ni/La₂O₃-LOC, which means that more exposed nickel active sites can participate in the activation and dissociation of methane. On the other hand, the difference in CO₂ conversion between the two catalysts could result from the higher amount of medium-strength basic sites in 5Ni/La₂O₃-LOC as evidenced by CO₂-TPD (Fig. 3 and Table 3) [11]. With regard to 5Ni/La₂O₃-LOC, its turnover frequency (TOF) of methane (12.8 s⁻¹) is the same as that of 5Ni/La₂O₃-C (12.9 s⁻¹) (Table 4), indicating

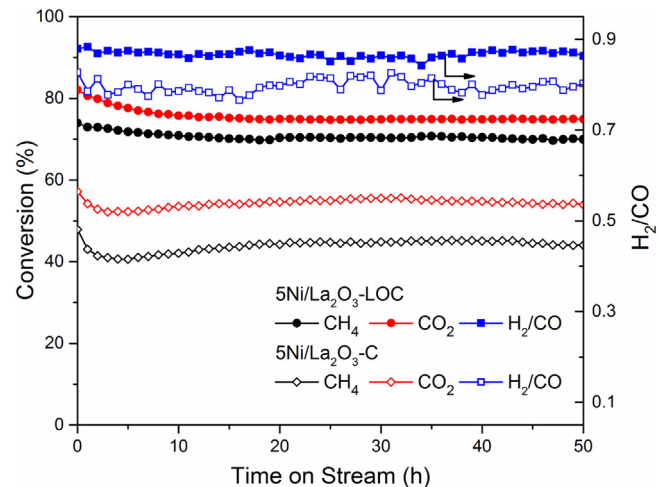


Fig. 7. Stability of the catalysts. CH₄ and CO₂ conversions as a function of time on stream over the catalysts including relevant H₂/CO ratio. Reaction conditions: CH₄/CO₂/N₂ = 15/15/70, GHSV = 60,000 mL h⁻¹ g_{cat}⁻¹, 700 °C, 1 atm.

that nature of active sites does not change for CH₄ conversion. It has been confirmed by TEM (Fig. 4) that nickel particles on both catalysts expose (111) facets. However, the CH₄ conversion rate of 5Ni/La₂O₃-LOC is much higher than that of 5Ni/La₂O₃-C. The difference in CH₄ conversion of the both catalysts is mainly ascribed to the different nickel dispersion. Additionally, 5Ni/La₂O₃-LOC has higher CH₄ conversion rate than that of nanocast-Ni/La₂O₃ reference catalyst [37], which uses SBA-15 as a template to enhance surface area thus improving nickel dispersion on La₂O₃. Therefore, nanorod-shaped support of 5Ni/La₂O₃-LOC can highly disperse nickel particles and then largely increase exposed active sites so that 5Ni/La₂O₃-LOC has higher activity than that of 5Ni/La₂O₃-C.

Stability tests are carried out to investigate the performance of the catalysts over a long time (Fig. 7). For both catalysts, distinct deactivation did not occur due to the stability of lanthanum oxide [61,62]. The promotional effect of La in catalytic stability has been reported in various reforming reactions [46,63]. Gallego et al. proposed the mechanism of Ni/La₂O₃ to eliminate carbon deposition [62]. During DRM process, CO₂ is adsorbed on La₂O₃ to form La₂O₂CO₃, and then La₂O₂CO₃ can react with Ni-CH_x species to produce CO and H₂ [34,36,64]. It can be noticed in Fig. 7 that the both catalysts keep stable after 50 h DRM reaction. Due to the poor nickel dispersion and large size of nickel particles, the exposed active sites on 5Ni/La₂O₃-C is much less than that on 5Ni/La₂O₃-LOC, so

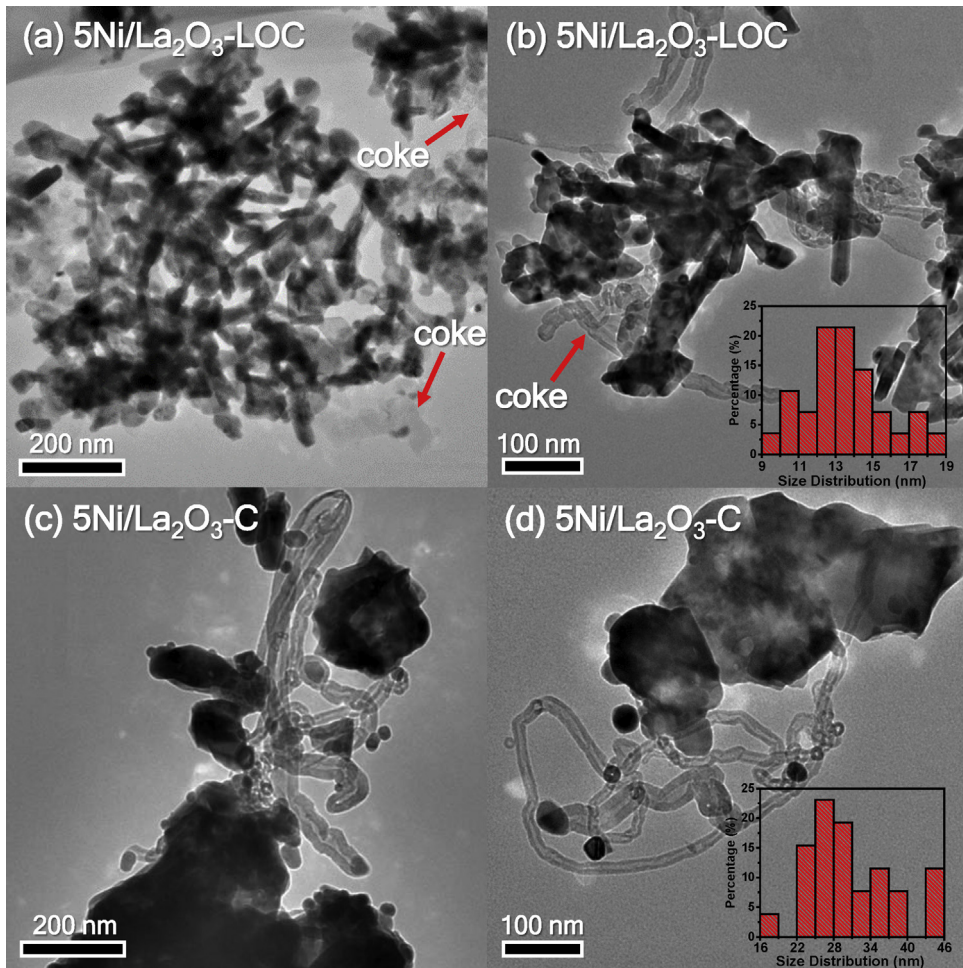


Fig. 8. TEM images of the spent (a,b) 5Ni/La₂O₃-LOC and (c,d) 5Ni/La₂O₃-C catalysts. (GHSV = 60,000 mL h⁻¹ g_{cat}⁻¹, 700 °C, Time on stream: 50 h).

that the CH₄ conversion of 5Ni/La₂O₃-C is much lower than that of 5Ni/La₂O₃-LOC. The selectivities of CO on both catalysts are higher than 99% (not shown) so that the ratio of H₂/CO in output gas is used to evaluate selectivities of gas products. With regard to 5Ni/La₂O₃-LOC, its ratio of H₂/CO keeps stable at around 0.87, which is higher than that of 5Ni/La₂O₃-C (0.80). Typically, H₂/CO ratio is mainly determined by RWGS, since the rate of RWGS is faster than CH₄ decomposition, and the latter is considered as the rate determining step for DRM [34,36,53]. Therefore, H₂/CO ratio can be raised mainly through adjusting operation conditions, such as increasing reaction temperature or making CH₄/CO₂ ratio well above 1 [18,65]. In addition, the deactivation in the initial period for 5Ni/La₂O₃-C is much faster than that of 5Ni/La₂O₃-LOC. Since the CH₄ dissociation and coke formation take place on surfaces of Ni particles [66], the difference in CH₄ conversion between the two catalysts is associated with different coke behavior caused by different degree of nickel dispersion on catalysts, which will be discussed in the following sections.

Additionally, the Weisz-Prater criterion (C_{WP}) and the Mears criterion are calculated (see the Supplementary information) to measure the mass and heat transfer limitations for the highest rates in the DRM. The value of C_{WP} (Eq. (10)) is 1.9×10^{-2} (<1) and 3.1×10^{-2} for CH₄ and CO₂ respectively. Since both of the values of C_{WP} are far less than 1, there are no internal diffusion limitations here [67–69]. Moreover, the value of the Mears criterion (Eq. (11)) is 1.30×10^{-5} and 2.12×10^{-5} (<3) for CH₄ and CO₂ respectively, which indicates that both of heat transfer (including interphase and

intraparticle) and mass transport limitations have been removed here [67,69,70].

$$C_{WP} = \frac{-r' A_{(obs)} \rho_c R^2}{D_e C_{As}} < 1 \quad (10)$$

$$\frac{-r' A R^2}{C_{Ab} D_e} < \frac{1 + 0.33\gamma\chi}{|n - \gamma_b \beta_b|(1 + 0.33n\omega)} \quad (11)$$

3.4. Characterization of spent catalysts

Fig. 8 displays TEM images of two spent catalysts recorded after 50 h DRM stability tests. For spent 5Ni/La₂O₃-LOC in Fig. 8a and b, nanorod-shape is maintained and coke forms in the periphery of the catalyst. While for spent 5Ni/La₂O₃-C, it can be observed in Fig. 8c and d that many Ni particles migrate out of the support due to growth of filamentous carbon and large Ni particles (~50 nm) form after 50 h DRM reaction. The average size of Ni particles on spent 5Ni/La₂O₃-LOC is 13.8 nm, while that on spent 5Ni/La₂O₃-C is 30.1 nm (Table 2). Typically, Ni(111) facets from step sites are considered as active sites for carbon nanofiber growth, and nickel particles with smaller size have a lower rate of carbon formation [71,72]. In addition, large morphology rearrangements take place on nickel particles during graphite whisker growth [71]. Therefore, 5Ni/La₂O₃-LOC exhibits excellent anti-sintering property due to its enhanced interaction between Ni and La₂O₃.

XRD patterns in Fig. 9 indicates the crystal transformation of spent catalysts. After 50 h DRM reaction, the support of spent 5Ni/La₂O₃-C is predominantly La₂O₂CO₃. While the support of

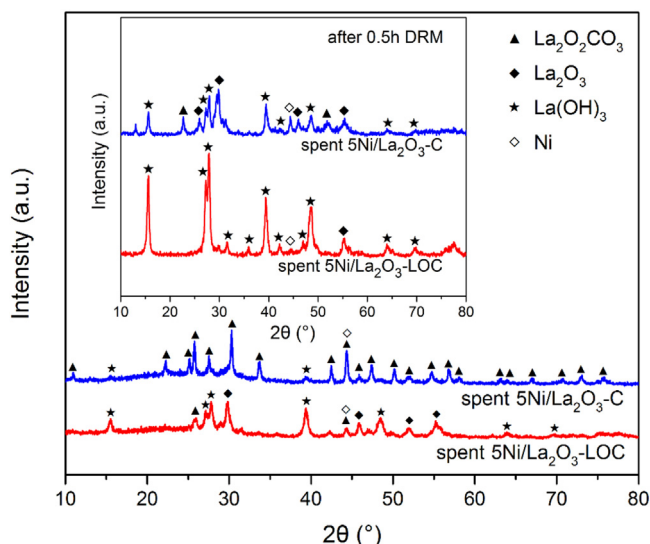


Fig. 9. XRD patterns of the spent catalysts and catalysts at initial period (inset). (GHSV = 60,000 mL h⁻¹ g_{cat}⁻¹, 700 °C, Time on stream: 50 h).

spent 5Ni/La₂O₃-LOC still consists of La₂O₃ mixed with La(OH)₃, and only a small amount of La₂O₂CO₃ can be detected. For 5Ni/La₂O₃-C, its intrinsic drawback is the poor nickel dispersion on the support. The minority of La₂O₃ is close to Ni particles where Ni particles dispersion is relatively dense so that coke deposits rapidly and lifts Ni particles to migrate out of the support. However, the majority of La₂O₃ is away from Ni particles where Ni particle dispersion is relatively sparse, so that La₂O₂CO₃ largely accumulates since they cannot react with deposited coke to regenerate La₂O₃. As for 5Ni/La₂O₃-LOC, on account of its prominently higher nickel dispersion as characterized by H₂ chemisorption (Table 2) and EELS (Fig. 5), La₂O₂CO₃ formed on the 5Ni/La₂O₃-LOC can react with deposited coke on neighbouring Ni particles timely so that negligible accumulation of La₂O₂CO₃ takes place. Additionally, it can be observed in the inset of Fig. 9 that La₂O₂CO₃ can quickly accumulate on 5Ni/La₂O₃-C only after 0.5 h DRM reaction while La₂O₂CO₃ is absent on XRD patterns of 5Ni/La₂O₃-LOC after 0.5 h DRM reaction. This also indicates that nickel dispersion on 5Ni/La₂O₃-LOC is better than that on 5Ni/La₂O₃-C. It should be noted that the diffraction peak of (111) facet of metallic nickel ($2\theta = 44.5^\circ$, JCPDF: 04-0850) is close to the diffraction peak of (110) facet of hexagonal La₂O₂CO₃ ($2\theta = 44.4^\circ$, JCPDF: 37-0804) and it is hard to differentiate these two peaks. Thus the characterization of Ni particle size after stability test mainly relies on size distribution of TEM images (Fig. 8).

The amount of coke deposition is measured from the TGA profiles as shown in Fig. 10. The mass increment in initial period during 200–350 °C corresponds to oxidation of nickel particles supported on spent catalysts. For both spent catalysts, mass loss at higher than 700 °C is ascribed to the decomposition of the reserved La₂O₂CO₃ as confirmed by XRD (Fig. 9). Apart from these parts of mass loss, the mass loss assigned to coke of spent 5Ni/La₂O₃-C is 1.2%, and that of spent 5Ni/La₂O₃-LOC is 10.3%. On account of the fact that 5Ni/La₂O₃-LOC has higher nickel dispersion and attains higher CH₄ conversion, higher total amount of coke on spent 5Ni/La₂O₃-LOC is reasonable. Results of quantitative calculation of carbon deposition on spent catalysts are listed in Table 5. Here, the averages of H₂ uptakes between reduced catalysts and spent catalysts were used to calculate the TOF of coke formation. It can be found that TOFs of methane conversion (Table 4) and coke formation (Table 5) on both catalysts are the same with each other, which means that the nature of nickel particles on both catalysts remain the same. It can be assumed that the difference in catalytic performance is

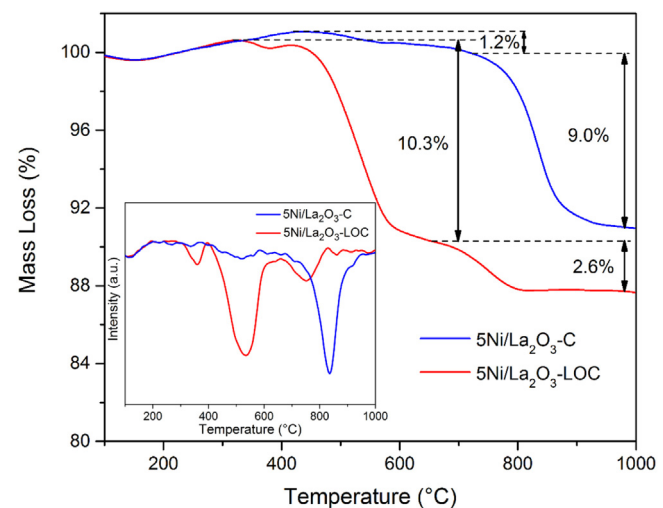


Fig. 10. TGA profiles and DTG profiles (inset) for the spent catalysts. (GHSV = 60,000 mL h⁻¹ g_{cat}⁻¹, 700 °C, Time on stream: 50 h).

mainly attributed to the improved nickel dispersion [37], which may also affect the type of coke on catalysts. Therefore, further characterizations to investigate the nature distinction of deposited coke between the two catalysts are necessary.

3.5. Coke formation analysis

Montero et al. investigated coke evolution on Ni/La₂O₃- α Al₂O₃ catalyst applied in ESR process [45]. They found that as reforming reaction steps into different periods, the change in the coke mechanism eventually leads to the change in the coke nature. In initial DRM reaction period, La₂O₂CO₃ rapidly accumulates on the 5Ni/La₂O₃-C while La₂O₂CO₃ is absent on the 5Ni/La₂O₃-LOC (inset of Fig. 9), indicating the biggest difference in coke nature might have occurred at early stage. Therefore, reaction conditions are altered in order to investigate difference in coke nature at early stage.

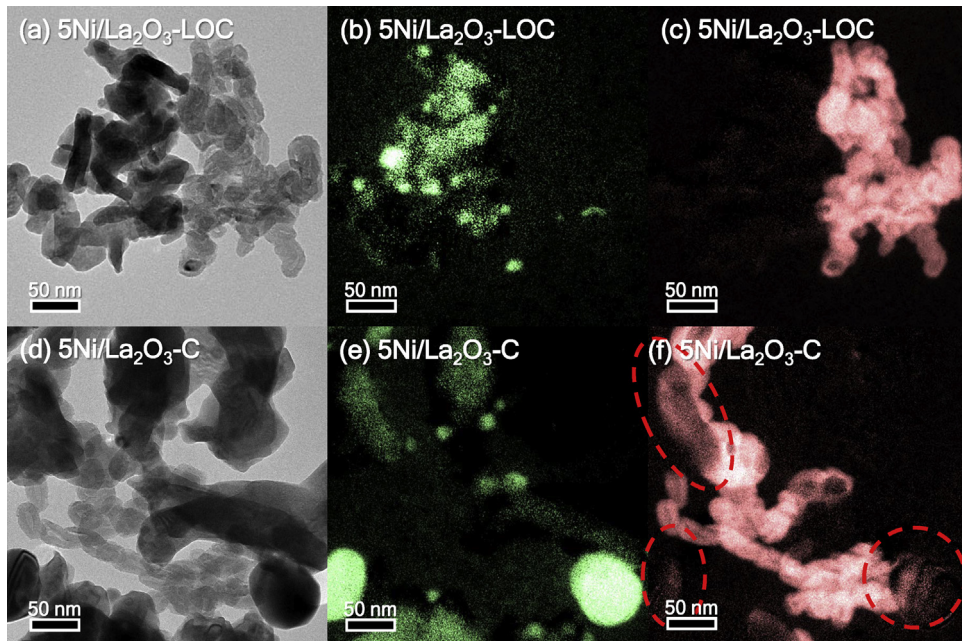
EELS technique is adopted to study the element distribution of the two catalysts after the DRM reaction for 20 h under lower GHSV (30,000 mL h⁻¹ g_{cat}⁻¹). Regions with dense coke accumulation are specially recorded in order to investigate coke behavior of the two catalysts. It can be seen in Fig. 11a–c that for 5Ni/La₂O₃-LOC, the nickel elemental distribution has a clear boundary with carbon elemental distribution, and coke is hardly found on the surface of the catalyst located on the left half of Fig. 11a–c. Only sparsely distributed single red pixels can be found on the surface of the catalyst, which refers to carbon element of La₂O₂CO₃. Additionally, the formation of filamentous coke on the right half of Fig. 11a–c could be ascribed to a few nickel particles located at the tip of filamentous coke, but the majority of nickel particles are free from coke. Besides, it should be noted that the amount of coke on 5Ni/La₂O₃-LOC has decreased and approached to that on 5Ni/La₂O₃-C under lower GHSV for 20 h (Fig. 12). While for 5Ni/La₂O₃-C, non-filamentous coke is observed on large nickel particles (~100 nm), which covers the surface of nickel particles and negatively affects catalyst activity as shown in Table 2 and Fig. 7. Montero et al. reported that coke resulted from CO disproportion and methane decomposition belongs to filamentous coke [45], which will not cause catalyst deactivation. However, filamentous coke can transform into non-filamentous coke with time on stream, which will deactivate catalysts [45].

TPO profiles are exhibited in Fig. 12 to investigate the amount and oxidation temperature of deposited coke on spent catalysts. It should be mentioned that no CO is formed during the entire experimental process. For 5Ni/La₂O₃-LOC, there is a main peak centered

Table 5

Quantitative calculation of carbon deposition on spent catalysts.

Sample	Weight loss (%) ^a	Coke/CH ₄ converted (mmol/mol)	H ₂ uptakes (mmol/g _{cat}) ^b	Coke formation rate		Carbon balance%
				mmol g _{cat} ⁻¹ s ⁻¹	TOF (s ⁻¹)	
5Ni/La ₂ O ₃ -C	1.2/9.0	0.12	0.80 × 10 ⁻³ /0.29 × 10 ⁻³	6.19 × 10 ⁻⁶	5.7 × 10 ⁻³	99.8
5Ni/La ₂ O ₃ -LOC	10.3/2.6	0.70	5.13 × 10 ⁻³ /4.65 × 10 ⁻³	5.47 × 10 ⁻⁵	5.6 × 10 ⁻³	99.8

^a Determined by TGA, weight loss corresponding to the oxidation of coke/the decomposition of La₂O₂CO₃.^b Determined by H₂ pulse chemisorption, reduced catalyst/spent catalyst after 50 h DRM reaction.**Fig. 11.** TEM images and corresponding EELS mapping of the reduced catalysts, with green pixels for nickel element and red pixels for carbon element. (a–c) 5Ni/La₂O₃-LOC (d–f) 5Ni/La₂O₃-C. (GHSV = 30,000 mL h⁻¹ g_{cat}⁻¹, 700 °C, Time on stream: 20 h). (For interpretation of the references to colour in this figure legend, the reader is referred to the web version of this article.)

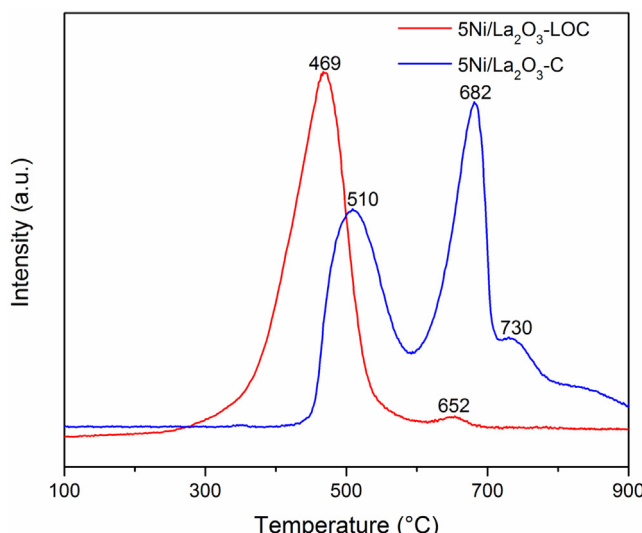
at 469 °C corresponding to filamentous coke gasification and a low peak centered at 652 °C assigned to non-filamentous coke gasification [73]. While for 5Ni/La₂O₃-C, the peak centered at 510 °C is ascribed to filamentous coke oxidation, which is higher than that on 5Ni/La₂O₃-LOC. In addition, the peak centered at 682 °C

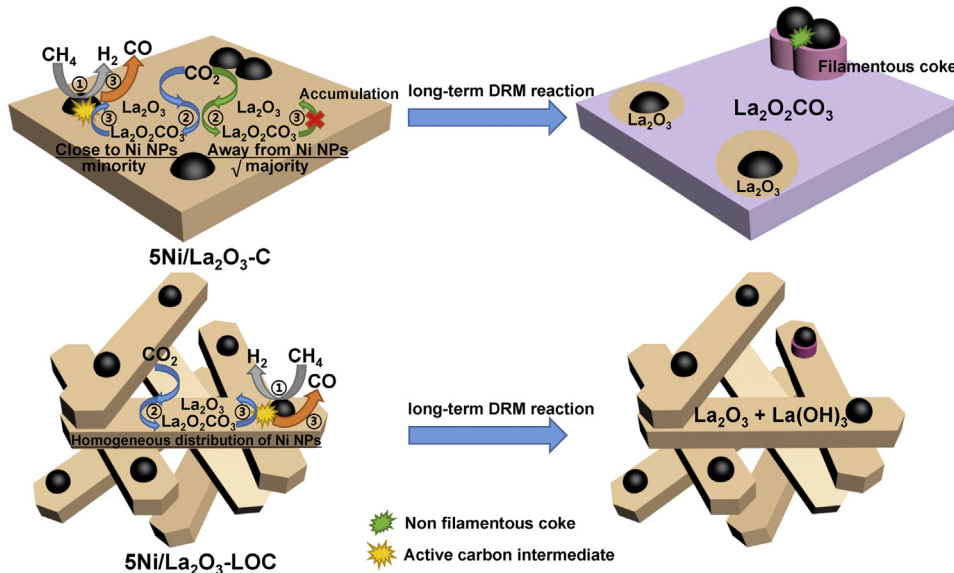
is assigned to non-filamentous coke gasification, while the peak on 5Ni/La₂O₃-LOC which corresponds to non-filamentous coke gasification is negligible. Moreover, the peak centered at 730 °C refers to the decomposition of reserved La₂O₂CO₃. It has been reported that transformation from filamentous coke to non-filamentous coke results from accumulation of filamentous coke with time on stream [45]. And it can be noticed in Fig. 11d–f that the accumulation of filamentous coke takes place in Ni particles concentrated regions caused by poor Ni dispersion of 5Ni/La₂O₃-C.

Raman spectra was recorded to understand the graphitic degree of coke on both spent catalysts at different reaction stages as shown in Fig. 13. The Raman spectra displays two main peaks at 1350 and 1600 cm⁻¹, which are ascribed to D band and G band respectively. D band is characteristic of disordered aromatic structures, while G band refers to condensed, ordered or graphitic aromatic structures [45,74]. It can be observed that the ratio of band intensities (I_G/I_D) representing graphitic degree of coke increases with time on stream for both catalysts. While at the same reaction stage, the I_G/I_D of 5Ni/La₂O₃-LOC is obviously lower than that of 5Ni/La₂O₃-C, indicating coke accumulation on 5Ni/La₂O₃-LOC is relieved compared with 5Ni/La₂O₃-C.

4. Discussion

Based on all the aforementioned results, a scheme of the catalyst models and their reaction mechanisms is proposed in Scheme 1. For both Ni/La₂O₃ catalysts, CH₄ activation and dissociation take place on the surface of Ni particles to form H₂ and active carbon inter-

**Fig. 12.** TPO profiles of the spent catalysts. (GHSV = 30,000 mL h⁻¹ g_{cat}⁻¹, 700 °C, Time on stream: 20 h).



Scheme 1. Scheme of the catalyst models and reaction mechanisms in the DRM process.

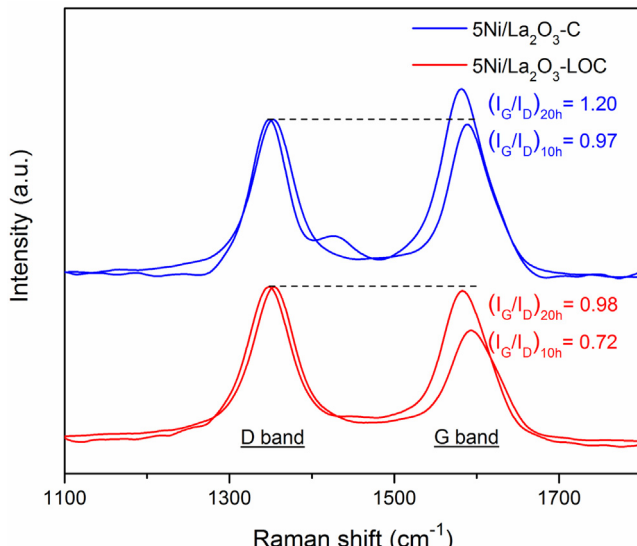


Fig. 13. Raman spectra of the spent catalysts. ($\text{GHSV} = 30,000 \text{ mL h}^{-1} \text{ g}_{\text{cat}}^{-1}$, 700°C).

mediate species [61,62]. CO_2 adsorbs on La_2O_3 to form $\text{La}_2\text{O}_2\text{CO}_3$ which can react with neighbouring active carbonaceous intermediate species to produce CO and regenerate La_2O_3 , completing the cycle between $\text{La}_2\text{O}_2\text{CO}_3$ and La_2O_3 . Herein, $\text{La}_2\text{O}_2\text{CO}_3$ can be also used as an indicator to reflect the degree of active metal dispersion on La_2O_3 support. It should be noted that $\text{La}_2\text{O}_2\text{CO}_3$ formed during reaction process can merely react with coke on the interface between nearby Ni particles and support [62,64]. If metal dispersion is good, $\text{La}_2\text{O}_2\text{CO}_3$ will timely participate to eliminate coke, while $\text{La}_2\text{O}_2\text{CO}_3$ will accumulate if metal dispersion is poor.

On account of uneven nickel dispersion (Fig. 5) and lower nickel surface area (Table 2) of $5\text{Ni/La}_2\text{O}_3\text{-C}$, the majority of La_2O_3 are away from Ni NPs so that the formed $\text{La}_2\text{O}_2\text{CO}_3$ cannot react with active carbon intermediate and largely accumulates and then covers the majority of support after long-term DRM reaction (Fig. 9). As for the minority of La_2O_3 close to Ni NPs, overly dense distribution of Ni NPs leads to rapid growth of filamentous coke (Fig. 11). Simultaneously, the mismatch between excessive growth of filamentous coke and limited La_2O_3 attending carbon elimination

leads to coke accumulation, which leads to the transformation from filamentous coke to non-filamentous coke (Figs. 12 and 13) [45]. Non-filamentous coke can cover nickel active sites and cause the loss of active sites during DRM process (Fig. 11 and Table 2).

While for $5\text{Ni/La}_2\text{O}_3\text{-LOC}$, it has higher nickel surface area upon reduction without occurrence of sintering thus exhibiting higher CH_4 conversion. In addition, its uniform nickel dispersion leads the coke elimination effect of La_2O_3 to be consistent with the growth of filamentous coke on nearby Ni particles. It can be seen in Fig. 11a–c that the majority of nickel particles are free from coke and coke deposition occurs on only a few nickel particles. Therefore, coke accumulation on $5\text{Ni/La}_2\text{O}_3\text{-LOC}$ is relatively relieved and the formation of non-filamentous coke is negligible. In addition, compared with $5\text{Ni/La}_2\text{O}_3\text{-C}$, $5\text{Ni/La}_2\text{O}_3\text{-LOC}$ possesses more medium-strength basic sites, which promotes CO_2 adsorption and activation on the support.

5. Conclusions

We have demonstrated that $\text{Ni/La}_2\text{O}_3$ nanorod catalysts with stabilized Ni nanoparticles for DRM process has been prepared via a wet impregnation method. Nanorod-shaped $\text{La}_2\text{O}_2\text{CO}_3$ as support precursor can highly disperse Ni particles and the increased exposed Ni active sites can significantly enhance DRM activity compared with $\text{Ni/La}_2\text{O}_3$ catalyst synthesized through conventional routes. Upon reduction, $\text{La}_2\text{O}_2\text{CO}_3$ transforms to La_2O_3 mixed with $\text{La}(\text{OH})_3$ but the nanorod-shape maintains. Moreover, nanorod-shaped support provides more medium-strength basic sites to facilitate CO_2 adsorption and increase CO_2 conversion in DRM process. At 700°C , the prepared $\text{Ni/La}_2\text{O}_3$ catalyst keeps stable with 70% of CH_4 conversion and 75% of CO_2 conversion under high GHSV ($60,000 \text{ mL h}^{-1} \text{ g}_{\text{cat}}^{-1}$), and the ratio of H_2/CO reaches 0.87. Simultaneously, the enhanced interaction between Ni and La_2O_3 suppresses sintering of nickel particles. The improved nickel dispersion lowers the graphitic degree of deposited coke and inhibits formation of non-filamentous coke, which impairs the catalyst performance. And interestingly, $\text{La}_2\text{O}_2\text{CO}_3$ can act as an indicator to reflect degree of Ni dispersion on the catalysts. Therefore, the prepared $\text{Ni/La}_2\text{O}_3$ nanorod catalyst exhibits efficient and stable performance for 50 h on stream at 700°C during DRM process.

Acknowledgements

We acknowledge the National Key Research and Development Program of China (2016YFB0600900), the National Science Foundation of China (21525626, 21222604, 21376169), the Program for New Century Excellent Talents in University (NCET-10-0611), the Scientific Research Foundation for the Returned Overseas Chinese Scholars (MoE), and the Program of Introducing Talents of Discipline to Universities (B06006) for their generous support.

References

- [1] A. Albarazi, P. Beaunier, P. Da Costa, *Int. J. Hydrogen Energy* 38 (2013) 127–139.
- [2] D. Li, X. Li, J. Gong, *Chem. Rev.* (2016), <http://dx.doi.org/10.1021/acs.chemrev.6b00099>.
- [3] D. Pakhare, J. Spivey, *Chem. Soc. Rev.* 43 (2014) 7813–7837.
- [4] S. Kawi, Y. Kathiraser, J. Ni, U. Oemar, Z. Li, E.T. Saw, *ChemSusChem* 8 (2015) 3556–3575.
- [5] C.J. Liu, J. Ye, J. Jiang, Y. Pan, *ChemCatChem* 3 (2011) 529–541.
- [6] S.D. Angelis, L. Turchetti, G. Monteleone, A.A. Lemonidou, *Appl. Catal. B* 181 (2016) 34–46.
- [7] T.H. Nguyen, A. Łamacz, P. Beaunier, S. Czajkowska, M. Domański, A. Krztoń, T. Van Le, G. Djéga-Mariadassou, *Appl. Catal. B* 152–153 (2014) 360–369.
- [8] T.H. Nguyen, A. Łamacz, A. Krztoń, B. Liszka, G. Djéga-Mariadassou, *Appl. Catal. B* 182 (2016) 385–391.
- [9] T.H. Nguyen, A. Łamacz, A. Krztoń, A. Ura, K. Chalupka, M. Nowosielska, J. Rynkowski, G. Djéga-Mariadassou, *Appl. Catal. B* 165 (2015) 389–398.
- [10] A.G. Bhavani, W.Y. Kim, J.S. Lee, *ACS Catal.* 3 (2013) 1537–1544.
- [11] D. Pakhare, V. Schwartz, V. Abdelsayed, D. Haynes, D. Shekhawat, J. Poston, J. Spivey, *J. Catal.* 316 (2014) 78–92.
- [12] K.S. Ha, J.W. Bae, K.J. Woo, K.W. Jun, *Environ. Sci. Technol.* 44 (2010) 1412–1417.
- [13] C. Zhang, K.W. Jun, K.S. Ha, Y.J. Lee, S.C. Kang, *Environ. Sci. Technol.* 48 (2014) 8251–8257.
- [14] H. Lin, E. Van Wagner, R. Raharjo, B.D. Freeman, I. Roman, *Adv. Mater.* 18 (2006) 39–44.
- [15] F. Polo-Garzon, D. Pakhare, J.J. Spivey, D.A. Bruce, *ACS Catal.* 6 (2016) 3826–3833.
- [16] S.T. Oyama, P. Hacarlioglu, Y. Gu, D. Lee, *Int. J. Hydrogen Energy* 37 (2012) 10444–10450.
- [17] T.D. Gould, M.M. Montemore, A.M. Lubers, L.D. Ellis, A.W. Weimer, J.L. Falconer, J.W. Medlin, *Appl. Catal. A* 492 (2015) 107–116.
- [18] S. Gaur, D.J. Haynes, J.J. Spivey, *Appl. Catal. A* 403 (2011) 142–151.
- [19] R.K. Singh, A. Yadav, A. Agrawal, A. Shukla, S. Adak, T. Sasaki, R. Bal, *Appl. Catal. B* 191 (2016) 165–178.
- [20] S. Sokolov, E.V. Kondratenko, M.-M. Pohl, A. Barkschat, U. Rodemerck, *Appl. Catal. B* 113–114 (2012) 19–30.
- [21] F. Yagi, R. Kanai, S. Wakamatsu, R. Kajiyama, Y. Suehiro, M. Shimura, *Catal. Today* 104 (2005) 2–6.
- [22] S.M. Stagg-Williams, F.B. Noronha, G. Fendley, D.E. Resasco, *J. Catal.* 194 (2000) 240–249.
- [23] C. Carrara, J. Múnera, E.A. Lombardo, L.M. Cornaglia, *Top. Catal.* 51 (2008) 98–106.
- [24] J. Zhang, H. Wang, A. Dalai, *J. Catal.* 249 (2007) 300–310.
- [25] H. Tian, X. Li, L. Zeng, J. Gong, *ACS Catal.* 5 (2015) 4959–4977.
- [26] J. Wei, E. Iglesia, *J. Catal.* 224 (2004) 370–383.
- [27] J. Wei, E. Iglesia, *J. Phys. Chem. B* 108 (2004) 4094–4103.
- [28] J. Wei, E. Iglesia, *Phys. Chem. Chem. Phys.* 6 (2004) 3754–3759.
- [29] V.C.H. Kroll, H.M. Swaan, C. Mirodatos, *J. Catal.* 161 (1996) 409–422.
- [30] V.C.H. Kroll, H.M. Swaan, S. Lacombe, C. Mirodatos, *J. Catal.* 164 (1996) 387–398.
- [31] A.E. Castro Luna, M.E. Iriarte, *Appl. Catal. A* 343 (2008) 10–15.
- [32] S. Singh, D. Zubenko, B.A. Rosen, *ACS Catal.* 6 (2016) 4199–4205.
- [33] A. Tsoukalou, Q. Imtiaz, S.M. Kim, P.M. Abdala, S. Yoon, C.R. Müller, *J. Catal.* (2016), <http://dx.doi.org/10.1016/j.jcat.2016.03.018>.
- [34] V.A. Tsipouriari, X.E. Verykios, *Catal. Today* 64 (2001) 83–90.
- [35] V.A. Tsipouriari, X.E. Verykios, *J. Catal.* 187 (1999) 85–94.
- [36] X.E. Verykios, *Int. J. Hydrogen Energy* 28 (2003) 1045–1063.
- [37] M.M. Nair, S. Kaliaguine, F. Kleitz, *ACS Catal.* 4 (2014) 3837–3846.
- [38] A.N. Fatsikostas, D.I. Kondarides, X.E. Verykios, *Catal. Today* 75 (2002) 145–155.
- [39] G. Wu, S. Li, C. Zhang, T. Wang, J. Gong, *Appl. Catal. B* 144 (2014) 277–285.
- [40] R. Pereñiguez, V.M. González-DelaCruz, J.P. Holgado, A. Caballero, *Appl. Catal. B* 93 (2010) 346–353.
- [41] W.D. Zhang, B.S. Liu, C. Zhu, Y.L. Tian, *Appl. Catal. A* 292 (2005) 138–143.
- [42] H. Zhu, P. Zhang, S. Dai, *ACS Catal.* 5 (2015) 6370–6385.
- [43] G. Li, C. Peng, C. Zhang, Z. Xu, M. Shang, D. Yang, X. Kang, W. Wang, C. Li, Z. Cheng, J. Lin, *Inorg. Chem.* 49 (2010) 10522–10535.
- [44] L. Mo, K.K.M. Leong, S. Kawi, *Catal. Sci. Technol.* 4 (2014) 2107–2114.
- [45] C. Montero, A. Ochoa, P. Castaño, J. Bilbao, A.G. Gayubo, *J. Catal.* 331 (2015) 181–192.
- [46] H. Ma, L. Zeng, H. Tian, D. Li, X. Wang, X. Li, J. Gong, *Appl. Catal. B* 181 (2016) 321–331.
- [47] R. Carrera Cerritos, R. Fuentes Ramírez, A.F. Aguilera Alvarado, J.M. Martínez Rosales, T. Viveros García, I.R. Galindo Esquivel, *Ind. Eng. Chem. Res.* 50 (2011) 2576–2584.
- [48] X. Huang, C. Dang, H. Yu, H. Wang, F. Peng, *ACS Catal.* 5 (2015) 1155–1163.
- [49] Y.H. Hou, W.C. Han, W.S. Xia, H.L. Wan, *ACS Catal.* 5 (2015) 1663–1674.
- [50] H. Chen, H. Yu, F. Peng, H. Wang, J. Yang, M. Pan, *J. Catal.* 269 (2010) 281–290.
- [51] T. Wang, Y. Meng, L. Zeng, J. Gong, *Sci. Bull.* 60 (2015) 1009–1018.
- [52] C.H. Bartholomew, R.B. Pannell, *J. Catal.* 65 (1980) 390–401.
- [53] J.F. Múnera, S. Irusta, L.M. Cornaglia, E.A. Lombardo, D. Vargas Cesar, M. Schmal, *J. Catal.* 245 (2007) 25–34.
- [54] X. Zheng, H. Lin, J. Zheng, X. Duan, Y. Yuan, *ACS Catal.* 3 (2013) 2738–2749.
- [55] D. Li, L. Zeng, X. Li, X. Wang, H. Ma, S. Assabumrungrat, J. Gong, *Appl. Catal. B* 176–177 (2015) 532–541.
- [56] R. Pereñiguez, V.M. Gonzalez-delaCruz, A. Caballero, J.P. Holgado, *Appl. Catal. B* 123–124 (2012) 324–332.
- [57] B.M. Faroldi, J.F. Múnera, L.M. Cornaglia, *Appl. Catal. B* 150–151 (2014) 126–137.
- [58] B. Valle, B. Aramburu, A. Remiro, J. Bilbao, A.G. Gayubo, *Appl. Catal. B* 147 (2014) 402–410.
- [59] J. Song, Y. Sun, R. Ba, S. Huang, Y. Zhao, J. Zhang, Y. Sun, Y. Zhu, *Nanoscale* 7 (2015) 2260–2264.
- [60] F. Wang, R. Shi, Z.Q. Liu, P.J. Shang, X. Pang, S. Shen, Z. Feng, C. Li, W. Shen, *ACS Catal.* 3 (2013) 890–894.
- [61] G. Sierra Gallego, C. Batiot-Dupeyrat, J. Barrault, F. Mondragón, *Ind. Eng. Chem. Res.* 47 (2008) 9272–9278.
- [62] G. Sierra Gallego, F. Mondragón, J.-M. Tatibouët, J. Barrault, C. Batiot-Dupeyrat, *Catal. Today* 133–135 (2008) 200–209.
- [63] U. Oemar, Y. Kathiraser, L. Mo, X.K. Ho, S. Kawi, *Catal. Sci. Technol.* 6 (2016) 1173–1186.
- [64] Z. Zhang, X.E. Verykios, S.M. MacDonald, S. Affrossman, *J. Phys. Chem.* 100 (1996) 744–754.
- [65] P. Djinović, I.G. Osojnik Črnivec, B. Erjavec, A. Pintar, *Appl. Catal. B* 125 (2012) 259–270.
- [66] Z. Wang, X.M. Cao, J. Zhu, P. Hu, *J. Catal.* 311 (2014) 469–480.
- [67] S. Oyama, X. Zhang, J. Lu, Y. Gu, T. Fujitani, *J. Catal.* 257 (2008) 1–4.
- [68] P.B. Weisz, C.D. Prater, *Adv. Catal.* 6 (1954) 60390–60399.
- [69] H.S. Fogler, *Elements of Chemical Reaction Engineering*, fourth ed., U.S.A., 2006.
- [70] D.E. Mears, *Ind. Eng. Chem. Process Des. Dev.* 10 (1971) 541–547.
- [71] H.S. Bengaard, J.K. Nørskov, J. Sehested, B.S. Clausen, L.P. Nielsen, A.M. Molenbroek, J.R. Rostrup-Nielsen, *J. Catal.* 209 (2002) 365–384.
- [72] S. Helveg, C. Lopez-Cartes, J. Sehested, P.L. Hansen, B.S. Clausen, J.R. Rostrup-Nielsen, F. Abild-Pedersen, J.K. Nørskov, *Nature* 427 (2004) 426–429.
- [73] W. Donphai, K. Faungnawakij, M. Chareonpanich, J. Limtrakul, *Appl. Catal. A* 475 (2014) 16–26.
- [74] J. Zhang, F. Li, *Appl. Catal. B* 176–177 (2015) 513–521.